Geochemistry Geophysics Geosystems G3
AN ELECTRONIC JOURNAL OF THE EARTH SCIENCES
Published by AGU and the Geochemical Society

Article
Volume 9, Number 1
26 January 2008
Q01003, doi:10.1029/2007GC001677
ISSN: 1525-2027

Effect of three-dimensional slab geometry on deformation in the mantle wedge: Implications for shear wave anisotropy

Erik A. Kneller and Peter E. van Keken

Department of Geological Sciences, University of Michigan, 2534 CC Little Building, 1100 North University Avenue, Ann Arbor, Michigan 48109, USA (ekneller@umich.edu; keken@umich.edu)

[1] Shear-wave splitting observations from many subduction zones show complex patterns of seismic anisotropy that commonly have trench-parallel fast directions. Three-dimensional flow may give rise to trench-parallel stretching and provide an explanation for these patterns of seismic anisotropy. Along-strike variations in slab geometry produce trench-parallel pressure gradients and are therefore a possible mechanism for three-dimensional flow. In this study we quantify the effects of variable slab dip, curved slabs, oblique subduction, and slab edges on flow geometry and finite strain in the mantle wedge of subduction zones. Temperature, dynamic pressure, velocity, and strain are calculated with high-resolution three-dimensional finite element models. These models include temperature- and stress-dependent rheology and parameterized slab and trench geometry. Thick layers (20–60 km) with strong trench-parallel stretching are observed in the mantle wedge when slab geometry involves a transition to slab dip less than 15° or strong curvature in the slab. In these cases, strong trench-parallel stretching develops when flow lines have an oblique to trench-normal orientation. This suggests that trench-parallel seismically fast directions may not indicate trench-parallel flow lines in systems with large along-strike variations. An oblique component of stretching is confined to a 20–30 km layer above the slab in systems with oblique subduction. The effects of slab edges include strong toroidal flow and focusing in the mantle near slab edges and trench-parallel flow that extends 50–100 km into the core of the mantle wedge.

Components: 8135 words, 16 figures, 3 tables.

Keywords: three-dimensional subduction zone dynamics; shear wave splitting; non-Newtonian rheology.

Index Terms: 8162 Tectonophysics: Rheology: mantle (8033); 8413 Volcanology: Subduction zone processes (1031, 3060, 3613, 8170); 8120 Tectonophysics: Dynamics of lithosphere and mantle: general (1213).

Received 5 May 2007; **Revised** 12 August 2007; **Accepted** 18 October 2007; **Published** 26 January 2008.

Kneller, E. A., and P. E. van Keken (2008), Effect of three-dimensional slab geometry on deformation in the mantle wedge: Implications for shear wave anisotropy, *Geochem. Geophys. Geosyst.*, *9*, Q01003, doi:10.1029/2007GC001677.

1. Introduction

[2] Three-dimensional solid-state creep may play an important role in a variety of processes that occur in the mantle wedge of subduction zones. Three-dimensional flow may control along-strike geochemical trends observed in some arcs [*Ewart et al.*, 1998] and likely affects thermal structure, which is a fundamental control on arc magma genesis [*Ulmer*, 2001] and slab metamorphism [*Hacker et al.*, 2003]. Three-dimensional deformation may also control rock fabric development and patterns of seismic anisotropy [*Hall et al.*, 2000; *Park and Levin*, 2002; *Mehl et al.*, 2003]. The common observation of trench-parallel seismically

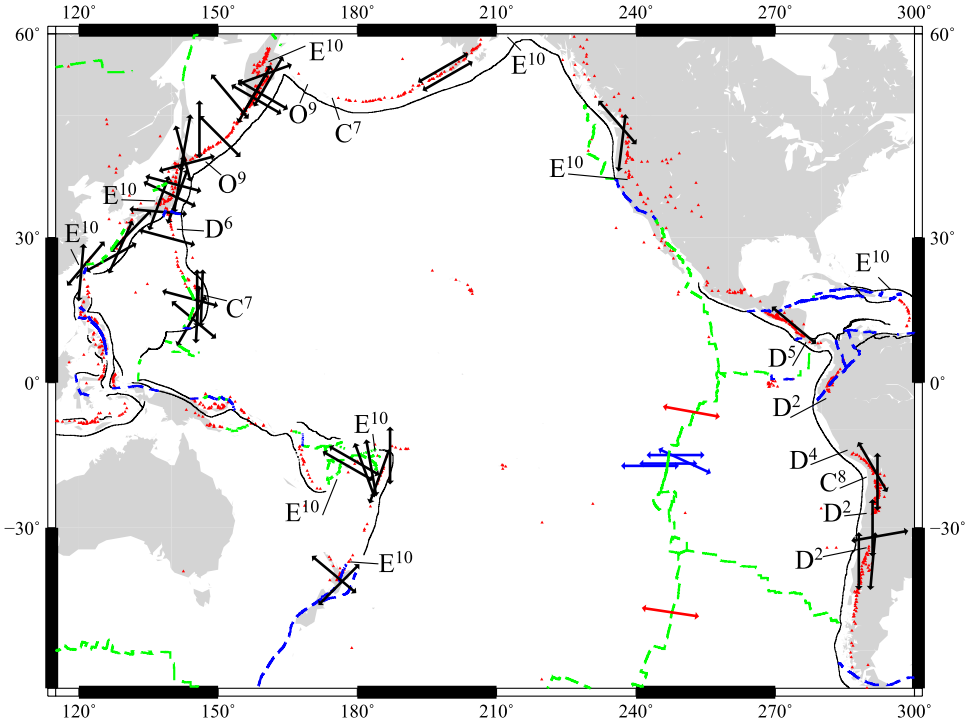

Figure 1. Seismic anisotropy around the Pacific Ring of Fire. Black arrows denote the fast directions of split local-S phases above subducting slabs (see auxiliary material Figures S1–S4). Blue arrows denote teleseismic shear wave splitting [*Wolfe and Solomon*, 1998]. Red lines show the fast direction measured from surface-wave and P_n tomography [*Park and Levin*, 2002]. Note that fast directions at spreading centers are consistently ridge normal (plate motion parallel), whereas at subduction zones fast directions are mostly trench-parallel or perpendicular to plate motion. Symbols denote regions with large along-strike variations in slab geometry and type of geometry: C denotes curved slabs, D represents variable dip, E denotes slab edges, and O refers to oblique subduction similar to case 9. Superscripts denote cases presented in this study with slab geometry that is applicable to a particular subduction system.

fast directions in subduction zones (Figure 1) has been used to infer the presence of a significant amount of trench-parallel stretching associated with trench-parallel flow in the mantle wedge. In this study we investigate the role of along-strike variations in slab geometry in producing three-dimensional flow and trench-parallel stretching in the mantle wedge.

[3] Two-dimensional cornerflow models of deformation in the mantle wedge predict strong stretching parallel to plate motion with maximum trench-normal stretching exceeding 500% [*McKenzie*, 1979; *Fischer et al.*, 2000] (Figure 2). Commonly observed varieties of olivine fabric show flow-parallel anisotropy with seismically fast directions that align parallel to the maximum stretch direction or approximately parallel to the flow direction for simple two-dimensional flow. The pattern of deformation shown in Figure 2 with flow-parallel olivine fabric will give rise to seismically fast directions that align parallel to the trench [*Ismaïl and Mainprice*, 1998]. Shear-wave splitting observations at most subduction zones show complex patterns of seismic anisotropy that are not consistent with this model [*Wiens and Smith*, 2003] (Figure 1 and auxiliary material Figures S1–S4).[1] These complex patterns commonly include abrupt rotations in seismically fast directions [*Polet et al.*, 2000; *Nakajima and Hasegawa*, 2004; *Anderson et al.*, 2004; *Long and van der Hilst*, 2005; *Nakajima et al.*, 2006] and trench-parallel fast splitting with maximum delay times around 1 s [*Smith et al.*, 2001; *Anderson et al.*, 2004; *Long and van der Hilst*, 2005, 2006]. Auxiliary material Figures S1–S4 show shear-wave splitting patterns and three-dimensional slab geometry in Pacific subduction systems.

[4] Several hypotheses have been proposed that provide an explanation for the common observation of trench-parallel seismically fast directions in

[1] Auxiliary materials are available in the HTML. doi:10.1029/2007GC001677.

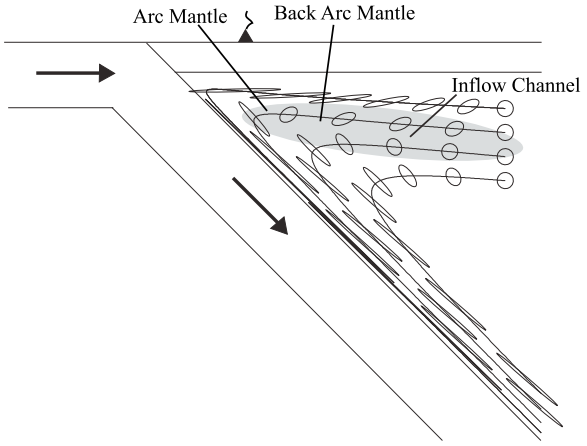

Figure 2. The evolution of finite strain ellipses along several streamlines for analytical cornerflow. Slab-driven flow produces a low-pressure corner and channelized return flow (gray region). The inflow channel is defined as a channel-like region where material flows from the back arc mantle to the arc mantle where dynamic pressure is relatively low. Note that flow lines in the core of the inflow channel are associated with relatively small amounts of shear and stretching. Strain geometry within this region will be most affected by trench-parallel pressure gradients.

the mantle wedge. These hypotheses use one of the following mechanisms: (1) olivine fabric transitions [*Katayama and Karato*, 2006; *Kneller et al.*, 2005, 2007; *Lassak et al.*, 2006], (2) preferred orientation of melt-filled cracks or melt networks [*Hiramatsu et al.*, 1998; *Fischer et al.*, 2000; *Holtzman et al.*, 2003], and (3) three-dimensional flow with commonly observed olivine fabric [*Hall et al.*, 2000; *Mehl et al.*, 2003; *Behn et al.*, 2007; *Lowman et al.*, 2007]. A transition to B-type olivine fabric with flow-normal seismically fast directions may provide an explanation for trench-parallel fast directions in the cold fore-arc mantle but is not applicable to the arc and back-arc mantle where temperature is high and deviatoric stress is low [*Kneller et al.*, 2005, 2007]. Melt-preferred orientation may play an important role beneath localized regions of melting such as active volcanic centers [*Hiramatsu et al.*, 1998]. Both the olivine-fabric-transition and melt-preferred orientation hypotheses assume that flow geometry is described by two-dimensional cornerflow and are applicable to relatively small regions of the mantle wedge.

[5] The three-dimensional flow hypothesis involves a significant deviation from simple cornerflow and the development of trench-parallel stretching. This hypothesis has potential to explain widespread trench-parallel shear-wave splitting in the hot arc and back-arc mantle of subduction zones. Candidate three-dimensional flow mechanisms include small-scale convection [*Honda et al.*, 2002; *Honda and Saito*, 2003; *Honda and Yoshida*, 2005; *Behn et al.*, 2007], differential slab rollback [*Russo and Silver*, 1994; *Mehl et al.*, 2003; *Anderson et al.*, 2004], oblique subduction [*Hall et al.*, 2000; *Mehl et al.*, 2003; *Honda and Yoshida*, 2005], trench-parallel motion of the overriding plate [*Hall et al.*, 2000], slab-edge effects [*Kincaid and Griffiths*, 2003; *Piromallo et al.*, 2006], large-scale mantle flow [*Smith et al.*, 2001; *Lowman et al.*, 2007], and variable slab geometry [*Hall et al.*, 2000]. Geodynamic modeling can be used to investigate the sensitivity of these mechanism to subduction parameters and applicability to specific subduction systems. However, a limited amount of work has been done in full three-dimensional geometry.

[6] Analogue experiments show that slab rollback is associated with limited trench-parallel stretching when slabs converge into the mantle [*Buttles and Olson*, 1998; *Kincaid and Griffiths*, 2003]. However, these experiments suggest that significant toroidal flow and trench-parallel stretching may occur close to slab edges. Recent numerical models of large-scale flow in subduction zones also show strong toroidal flow next to slab edges in addition to complicated flow in the mantle wedge [*Lowman et al.*, 2007]. Three-dimensional models of free convection in the mantle wedge suggest that water weakening [*Honda et al.*, 2002; *Honda and Saito*, 2003; *Honda and Yoshida*, 2005] and crustal foundering [*Behn et al.*, 2007] may give rise to three-dimensional flow beneath volcanic arcs. These models have yet to include three-dimensional finite strain calculations and fabric development, which makes it difficult to determine consequences for seismic anisotropy. [*Hall et al.*, 2000] demonstrated that back-arc shear zones may give rise to trench-parallel stretching and seismically fast directions. The isoviscous models implemented by *Hall et al.* [2000] did not include variable geometry.

[7] Models from previous studies of three-dimensional flow did not include olivine rheology nor realistic slab geometries with along-strike variability. These geometric variations include variable slab dip, curved trenches and truncated slabs. Qualitative predictions of the effects of variable slab dip and curved trenches can be obtained with isoviscous analytical methods [*Hall et al.*, 2000]. Analytical cornerflow solutions show that variable slab dip and curved trenches produce trench-

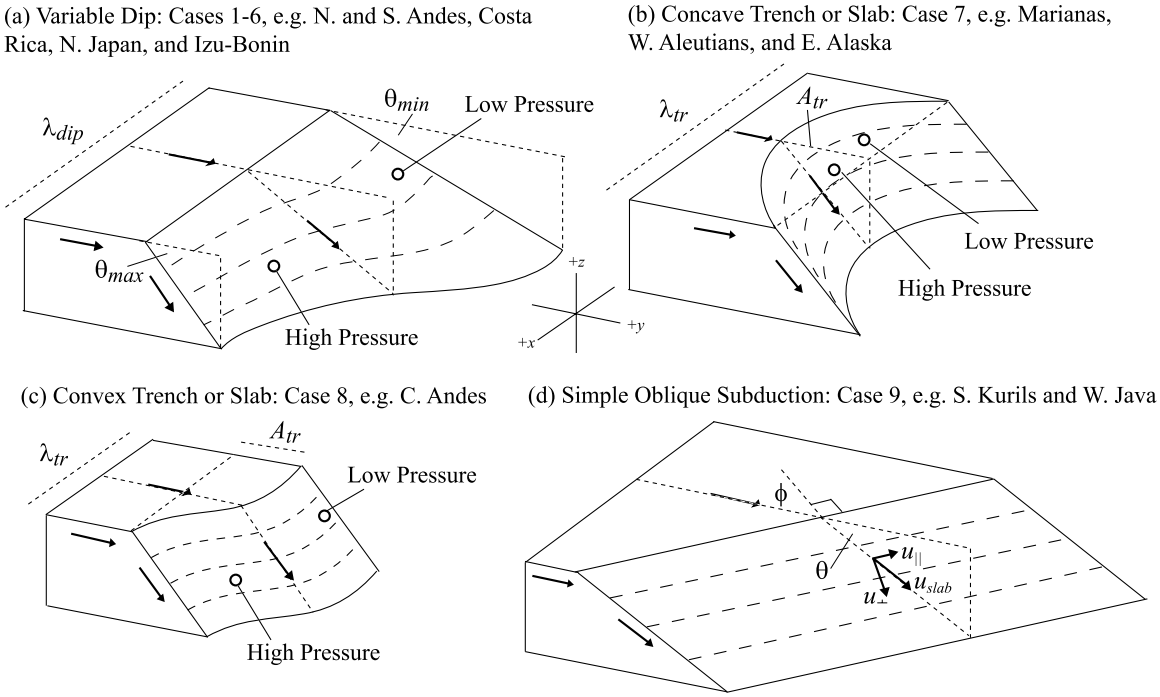

Figure 3. A variety of three-dimensional slab geometries are considered in this study: (a) variable slab dip, (b and c) curved trench or slabs, and (d) oblique subduction. Important geometric parameters are shown for each case (Table 1). Regions with relatively low and high pressure along the trench-parallel direction are denoted with open circles. The convergence direction is denoted with black arrows.

parallel variations in the geometry of the low-pressure region in the corner of the mantle wedge, which in turn generates trench-parallel pressure gradients and a component of trench-parallel flow. This low-pressure region is created as subducting slabs entrain and remove material from the corner of the mantle wedge and is associated with channelized flow toward the corner (Figure 2). Material traveling within the core of the inflow channel experiences minimum vertical shear and has the most potential to develop trench-parallel stretching when trench-parallel pressure gradients are present.

[8] The distance over which this low-pressure zone extends into the back arc is inversely proportional to slab dip. In subduction systems with variable slab dip, this distance varies along strike, which gives rise to trench-parallel pressure gradients that can generate a component of trench-parallel flow (Figure 3a). Curved slabs are also associated with along-strike pressure gradients which can generate radiating flow geometry that differs significantly from cornerflow flow (Figures 3b and 3c). Oblique subduction (Figure 3d) may also produce trench-parallel deformation in the mantle wedge by direct shear induced by the down-going slab. However, the distance over which oblique shear is transmitted into the wedge is strongly dependent on rheology. Trench-parallel pressure gradients are also located in the mantle near the low-pressure corner above slab edges.

[9] Although qualitative predictions can be obtained with isoviscous analytical methods, quantifying the magnitude of pressure gradients, flow geometry, and strain geometry in the mantle wedge requires three-dimensional numerical calculations with realistic rheology. In this study we show results from three-dimensional high-resolution subduction zone models with experimentally based olivine rheology and slab geometry defined with simple functions that approximate observed slab geometry. Specifically, we quantify flow geometry and trench-parallel strain associated with variable slab dip (Figure 3a) and curved slabs (Figures 3b and 3c). We also quantify trench-parallel strain accumulation for oblique subduction with straight trenches (Figure 3d) and flow geometry associated with slab edges. Our primary focus is on constraining the geometric parameters that give rise to significant trench-parallel stretching. This information is then used to determine the subduction systems where the pattern of deformation and structure of seismic anisotropy is mostly likely

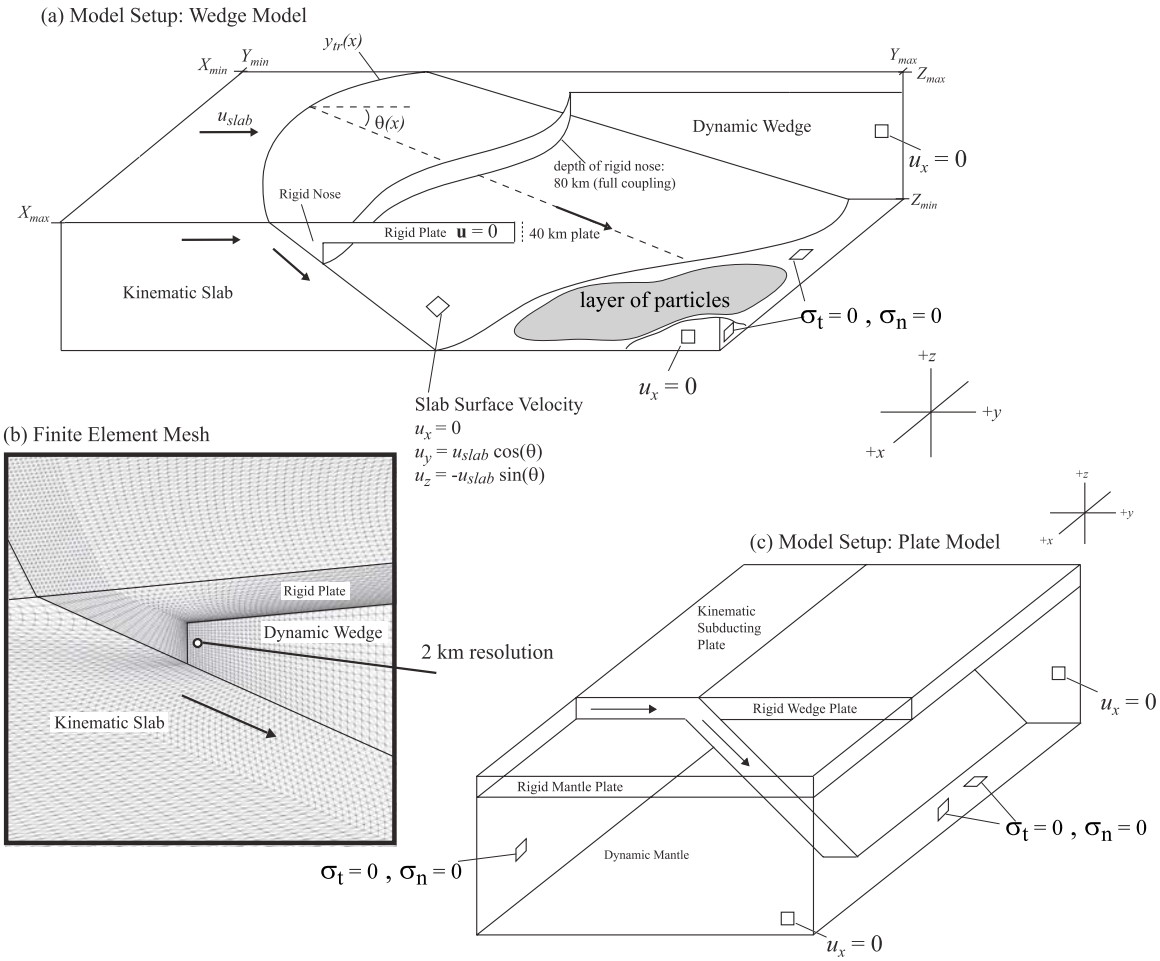

Figure 4. (a and c) Three-dimensional model setups and (b) finite element mesh.

affected by three-dimensional flow associated with variable geometry.

2. Modeling Approach

2.1. Thermomechanical Model

[10] We model slab-driven flow with a kinematic-dynamic approach where the subducting slab and overriding plate are treated as kinematic entities and flow in the mantle wedge is driven by velocity boundary conditions at the surface of the slab [*van Keken et al.*, 2002; *Kneller et al.*, 2005, 2007]. The model domain is a Cartesian box with a depth of 300 km and is divided into three parts: (1) kinematic slab, (2) kinematic overriding plate with 40 km thick conductive lid and rigid corner, and (3) dynamic mantle wedge (Figure 4a). The side boundaries of this box are parallel to the y axis of the Cartesian reference system. For all cases considered in this study, the convergence direction of the in-coming plate is parallel to the side boundaries (i.e., y axis). The rigid corner limits advection in the fore-arc mantle, which is necessary to produce a reasonable match with heat flow and seismic attenuation observations [*Kneller et al.*, 2007]. For all cases, the rigid corner extends down to a constant depth of 80 km (Figure 3a).

[11] A parameterized slab geometry is implemented that includes both variable slab dip and trench curvature (Figure 4a). The y coordinate of the trench y_{tr} and slab dip θ in the y direction depend only on the x coordinate (i.e., convergence-normal direction). For all cases presented in this work, the slab dips in the $+y$ direction. The parameterized slab geometries considered in this study and model dimensions are described in Figure 3 and Tables 1 and 2.

[12] Fluid flow in the dynamic wedge is governed by the conservation of momentum and mass for an incompressible infinite Prandtl number fluid with-

Table 1. Parameterized Slab Models

Case	$y_{tr}(x)$ km	$\theta(x)^\circ$
1, 2, 3, and 4	$y_{tr} = 0$	$\theta(x) = \theta_{\max} - \frac{A_{dip}}{2}\left[\sin\left(\pi\frac{(x-x_{\min})}{\lambda_{dip}} + \frac{\pi}{2}\right) + 1\right]$, where $\lambda_{dip} = x_{\max} - x_{\min}$ and $A_{dip} = \theta_{\max} - \theta_{\min}$
5	$y_{tr} = 0$	$\theta(x) = \theta_{\min} + \frac{A_{dip}}{2}\left[\sin\left(\pi\frac{(x-x_{\min})}{\lambda_{dip}} + \frac{\pi}{2}\right) + 1\right]$, where $\lambda_{dip} = x_{\max} - x_{\min}$ and $A_{dip} = \theta_{\max} - \theta_{\min}$
6	$y_{tr} = 0$	$\theta(x) = \theta_{\min} + \frac{A_{dip}}{2}\left[\sin\left(\pi\frac{(x-x_{mid})}{\lambda_{dip}} + \frac{\pi}{2}\right) + 1\right]$, where $\lambda_{dip} = x_{\max} - x_{mid}$, $A_{dip} = \theta_{\max} - \theta_{\min}$, $x_{mid} = \frac{x_{\max}+x_{\min}}{2}$ and $\theta(x) = \theta_{\max}$ when $x < x_{mid}$
7	$y_{tr} = -A_{tr}\sin\left(\pi\frac{(x-x_{\min})}{\lambda_{tr}}\right) + 500$, where $\lambda_{tr} = x_{\max} - x_{\min}$	$\theta(x) = 60$
8	$y_{tr} = \frac{A_{tr}}{2}\left[\cos\left(\pi\frac{(x-x_{\min})}{\lambda_{tr}} + 1\right]\right.$, where $\lambda_{tr} = x_{\max} - x_{\min}$	$\theta(x) = 45$
9	$y_{tr} = -\tan(\phi)x + \tan(\phi)x_{\max}$	$\theta(x) = 25.31$
10	$y_{tr} = 500$ km	$\theta(x) = 45$

out body forces. The conservation of momentum is expressed as

$$-\nabla P + \nabla\cdot(\eta\dot{\epsilon}) = 0 \quad (1)$$

where $\dot{\epsilon}$ is the strain rate tensor, η is effective viscosity, and P is dynamic pressure. The conservation of mass is expressed as

$$\nabla\cdot\mathbf{u} = 0 \quad (2)$$

where $\mathbf{u}$ is velocity. No-slip boundary conditions are implemented along the base of the overriding plate and surface of the kinematic slab (Figure 4a). Velocity boundary conditions at the base of the overriding plate are set equal to zero. Velocity is parallel to the slab surface. The dip of velocity vectors is equal to the local dip of the subducting slab in the y direction. The convergence-normal velocity component u_x is equal to zero for all cases considered in this study. Convergence velocity u_{slab} is equal to 5 cm/a for all cases. Inflow-outflow boundary conditions with zero normal and tangential deviatoric stress are implemented along the back ($+y$) and bottom ($-z$) boundaries of the mantle wedge. Reflecting boundary conditions ($u_x = 0$) are used along the side ($+x$ and $-x$) boundaries. The effects of reflecting boundary conditions on deformation were investigated by

Table 2. Geometric Parameters

Case	Parameters for Slab Models	$x_{\min}$, $x_{\max}$, $y_{\min}$, $y_{\max}$, $z_{\min}$, $z_{\max}$, km
1	$\theta_{\min} = 20^\circ$, $\theta_{\max} = 30^\circ$, $\lambda_{dip} = 500$ km	0, 500, −300, 2000, −300, 0
2	$\theta_{\min} = 13^\circ$, $\theta_{\max} = 30^\circ$, $\lambda_{dip} = 500$ km	0, 500, −300, 2000, −300, 0
3	$\theta_{\min} = 20^\circ$, $\theta_{\max} = 30^\circ$, $\lambda_{dip} = 1000$ km	0, 1000, −300, 2000, −300, 0
4	$\theta_{\min} = 13^\circ$, $\theta_{\max} = 30^\circ$, $\lambda_{dip} = 1000$ km	0, 1000, −300, 2000, −300, 0
5	$\theta_{\min} = 30^\circ$, $\theta_{\max} = 60^\circ$, $\lambda_{dip} = 1000$ km	0, 1000, −300, 1000, −300, 0
6	$\theta_{\min} = 30^\circ$, $\theta_{\max} = 45^\circ$, $\lambda_{dip} = 500$ km	0, 1000, −300, 1000, −300, 0
7	$A_{tr} = 400$ km, $\lambda_{tr} = 900$ km	0, 900, −300, 1000, −300, 0
8	$A_{tr} = 250$ km, $\lambda_{tr} = 500$ km	0, 500, −300, 1000, −300, 0
9	$\phi = 35^\circ$	0, 1000, −300, 2000, −300, 0
10	plate thickness = 50 km	0, 1000, −250, 1000, −300, 0

Table 3. Model Parameters

Symbol	Description	Value
u_{slab}	convergence velocity	5 cm/a
η_o	reference viscosity	10^{18} Pas
$\eta_{\max}$	maximum viscosity	10^{26} Pas
A[a]	constant	$10^{-11.9}$ s^{-1} Pa^{-3}
E[b]	activation energy	510 kJ/mol
n	stress exponent	3.0[a]
R	gas constant	8.3145 J/K/mol
k	thermal conductivity	3 W/m/K
ρ	density	3300 kg/m^3
c_p	specific heat	1250 J/kg/K
Δt	dimensional time step	196,000 years
$t_{\max}$	maximum time	20 Ma

[a] *Karato and Jung* [2003].
[b] *Mei and Kohlstedt* [2000].

laterally extending the slab and mantle wedge. In general the reflecting boundary conditions have little effect on the pattern of strain but do increase strain rate in a zone that extends 50 km away from the side boundaries.

[13] A power-law rheology with experimentally based parameters for olivine aggregates is implemented in the viscous wedge:

$$\dot{\epsilon}_{ij} = A \exp\left[-\frac{E}{RT}\right]\sigma^{n-1}\sigma_{ij} \tag{3}$$

where $\dot{\epsilon}_{ij}$ is the ij-th component of the strain rate tensor, σ_{ij} is the ij-th component of the deviatoric stress tensor, σ is the second invariant of the deviatoric stress tensor, E is activation energy, T is temperature, R is the gas constant, n is the stress exponent, and A is a constant (Table 3). The second invariant of the stress tensor is defined as

$$\sigma = \sqrt{\frac{1}{2}\sum \sigma_{ij}\sigma_{ij}} \tag{4}$$

Effective viscosity is defined as

$$\eta = \frac{\sigma}{2\dot{\epsilon}} \tag{5}$$

where $\dot{\epsilon}$ is second invariant of the strain rate tensor:

$$\dot{\epsilon} = \sqrt{\frac{1}{2}\sum \dot{\epsilon}_{ij}\dot{\epsilon}_{ij}} \tag{6}$$

The effective viscosity for power-law rheology can be expressed in terms of strain rate

$$\eta_{disloc} = A^{-\frac{1}{n}} \exp\left[\frac{E}{nRT}\right]\dot{\epsilon}^{\frac{1-n}{n}} \tag{7}$$

Effective viscosity η is non-dimensionalized with a reference viscosity η_o and truncated with a maximum viscosity $\eta_{\max}$ (Table 3).

[14] The time-dependent heat advection-diffusion equation with constant conductivity is solved for the entire domain and is defined as:

$$\frac{\partial T}{\partial t} = \frac{k}{\rho c_p}\nabla^2 T - (\mathbf{u}\cdot\nabla)T \tag{8}$$

where T is temperature, t is time, k is thermal conductivity, c_p is specific heat, and ρ is density (Table 3). For simplicity we ignore the effects of radiogenic and frictional heating. Temperature is set equal to zero at the surface of the model. A half-space cooling model with a cooling age of 50 Ma defines the initial condition and essential boundary conditions along the $-y$ and $+y$ boundaries. Insulating boundary conditions are implemented along side boundaries (−x and +x), at the base of the model, and along the +y boundary of the mantle wedge. Velocity within the kinematic slab ($\mathbf{u}$) is parallel to the surface of the slab. Divergence within the subduction slab is equal zero with this velocity description. Model parameters are summarized in Table 3.

[15] The finite element package Sepran (http://ta.twi.tudelft.nl/sepran/sepran.html) is used to discretize equations (1), (2), and (8) on a grid composed of linear tetrahedra. The resulting system of equations are solve using the Bi-CGSTAB iterative method [*van der Vorst*, 1992]. For the solution of equations (1) and (2) we use modified Taylor-Hood elements with linear basis functions for both velocity and pressure [*Cuvelier et al.*, 1986]. Streamline-upwinding with the Petrov-Galerkin formulation is used for the solution of equation (8) [*van Keken et al.*, 2002]. Strong local refinement is implemented in the corner of the wedge with a minimum resolution of 2 km along vertical planes parallel to the convergence direction (Figure 4b). Convergence tests were performed by comparing solutions obtained on a grid with resolution less than 1 km to solutions obtained using coarser grids. These tests showed that this high resolution (<5 km) is necessary to obtain relative numerical errors less than 10–20% with velocity and temperature in the corner of the mantle wedge. Minimum resolution in the convergence-normal direction varies from 5–10 km. A maximum resolution of 15 km is implemented in the back-arc mantle. The implicit Euler scheme is used for time integration with a dimensional time step Δt equal to 196,000 years. This time step is approximately two times the ratio of average trench-normal grid spacing (5 km) over

maximum velocity. The stress-dependent rheology implemented in equation (7) requires a special iterative procedure. This involves repeatedly solving equations (1) and (2) at each time step until a relative error of 10^{-3} is obtained.

[16] Steady state solutions for velocity and temperature are reached in less than 15–20 Ma of subduction throughout most of the mantle wedge where advection is the dominant mode of heat transport (Figure 5). A comparison of output for a model with the non-Newtonian rheology and an isoviscous example is shown in Figure 6 (see Tables 1 and 2, case 2). These models involve a strong variation in slab dip and a duration of subduction equal to 20 Ma. Non-Newtonian rheology gives rise to higher temperature is the corner of the mantle wedge (Figures 6a and 6e), larger strain rates (Figures 6b and 6f), and larger flow speed (Figures 6c and 6g). Furthermore, the experimentally based non-Newtonian rheology is associated with trench-parallel flow velocity that is a factor of 3 larger than the isoviscous case (compare Figures 6d and 6h).

2.2. Olivine Fabric Model

[17] In this study we explore the hypothesis that trench-parallel seismically fast directions are caused by high-temperature varieties of lattice preferred orientation with stretching-parallel fast directions. We use finite strain as a proxy for the magnitude and orientation of olivine lattice preferred orientation. Dislocation creep, which is necessary for the development of lattice preferred orientation, is assumed to be the dominant deformation mechanism in the mantle wedge. Particle motion and finite strain are calculated using a 4th order Runge-Kutta scheme and the velocity field obtained after 20 Ma of subduction. With each case finite strain is calculated in particles that are initially distributed in a horizontal layer at a depth of 300 km (Figure 4a). This layer of particles has an initial spacing of 5 km and is traced through the flow field of the mantle wedge. A new layer of particles is injected into the base of the model every 200,000 years. This method accounts for strain accumulation throughout 75% of the upper mantle where most of the mantle's anisotropy is located and dislocation creep is thought to be the dominant deformation mechanism. The direction and magnitude of the principle stretch axes of finite strain ellipses are obtained by numerically solving the following equation

$$\frac{\partial}{\partial t}\mathbf{F} = \mathbf{L}\cdot\mathbf{F} \tag{9}$$

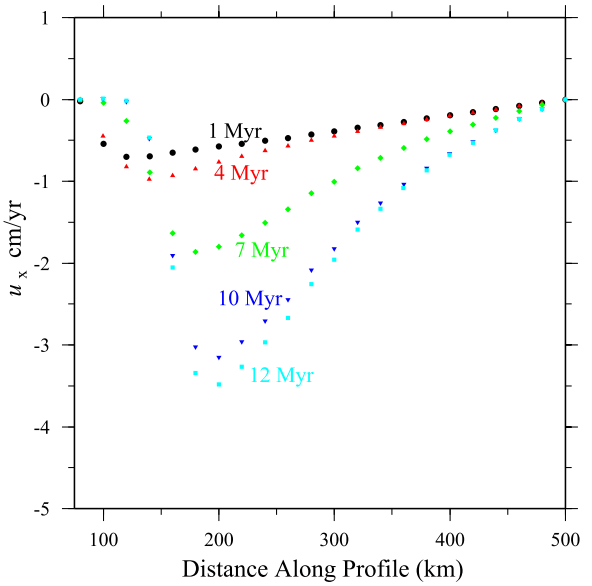

Figure 5. Trench-parallel velocity in the mantle wedge for case 2 (see Figure 7b) as a function of the duration of subduction. This profile is along the x direction at y = 400 km and z = −100 km (refer to Figure 8f). Steady state solutions for velocity, temperature, and pressure are obtained in less than 15–20 Ma throughout most of the mantle wedge.

where **L** is the velocity gradient tensor and **F** is the deformation gradient tensor [*McKenzie*, 1979; *Spencer*, 1980]. The velocity gradient tensor is defined as

$$\mathbf{L} = \begin{bmatrix} \frac{\partial v_x}{\partial x} & \frac{\partial v_x}{\partial y} & \frac{\partial v_x}{\partial z} \\ \frac{\partial v_y}{\partial x} & \frac{\partial v_y}{\partial y} & \frac{\partial v_y}{\partial z} \\ \frac{\partial v_z}{\partial x} & \frac{\partial v_z}{\partial y} & \frac{\partial v_z}{\partial z} \end{bmatrix} \tag{10}$$

where v_x, v_y, v_z are velocity components in the x, y, and z directions respectively. The deformation gradient tensor is defined as

$$\mathbf{F} = \begin{bmatrix} \frac{\partial s_x}{\partial x} + 1 & \frac{\partial s_x}{\partial y} & \frac{\partial s_x}{\partial z} \\ \frac{\partial s_y}{\partial x} & \frac{\partial s_y}{\partial y} + 1 & \frac{\partial s_y}{\partial z} \\ \frac{\partial s_z}{\partial x} & \frac{\partial s_z}{\partial y} & \frac{\partial s_z}{\partial z} + 1 \end{bmatrix} \tag{11}$$

where s_x, s_y, and s_z are components of displacement in the x, y, and z directions. The tensor **F** relates a particle's post-deformational position (x_f, y_f, z_f) to its initial position (x_o, y_o, z_o) excluding rigid translation.

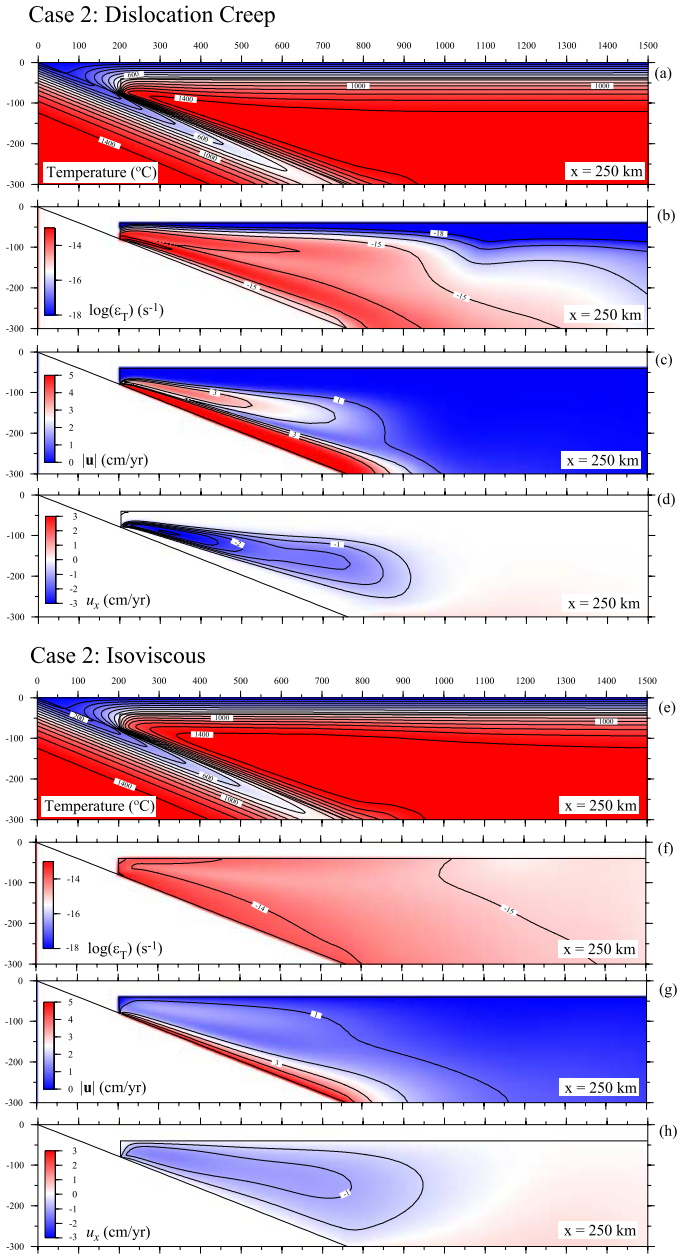

Figure 6. (a and e) Temperature, (b and f) strain rate, (c and g) magnitude of flow velocity, and (d and h) trench-parallel velocity for case 2 (see Figure 7b) obtained after 20 Ma of subduction. Cases are shown with both experimentally based non-Newtonian rheology for olivine aggregates and isoviscous rheology.

The following initial condition is used for the solution of equation (9):

$$\mathbf{F} = \begin{bmatrix} 1 & 0 & 0 \\ 0 & 1 & 0 \\ 0 & 0 & 1 \end{bmatrix} \tag{12}$$

In order to calculate finite strain, **F** must be related to the left Cauchy-Green tensor **B**

$$\mathbf{B} = \mathbf{F} \cdot \mathbf{F}^T \tag{13}$$

The eigenvectors of **B** are parallel to the principle stretch axes, which are denoted by $\mathbf{v}_{\min}$, $\mathbf{v}_{mid}$, and $\mathbf{v}_{\max}$. The magnitudes of the principle stretch axes of the finite strain ellipse ($\lambda_{\min}$, λ_{mid}, $\lambda_{\max}$) are equal to the square roots of the eigenvalues of **B** [*Spencer*, 1980].

[18] Experiments [*Zhang et al.*, 2000; *Katayama and Karato*, 2006] and natural observations [*Ismaïl and Mainprice*, 1998; *Skemer et al.*, 2006] show that at temperatures greater than 650–900°C seismically fast directions in deformed olivine aggre-

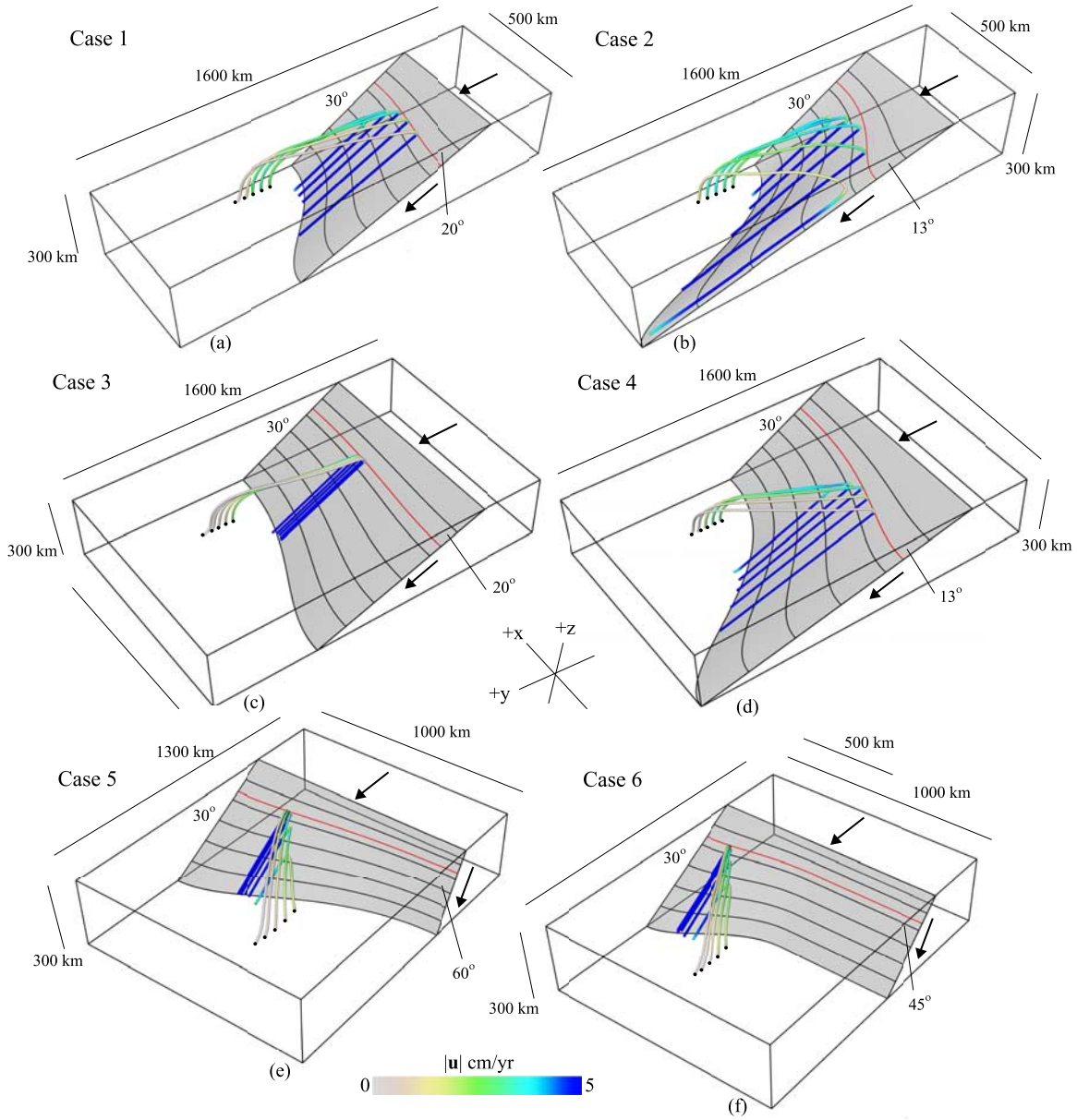

Figure 7. Slab geometry and flow lines for cases with along-strike variations in slab dip (cases 1–6). Flow lines are calculated for particles that were initially distributed parallel to the convergence direction (trench-normal) at the base of the model. Flow lines are colored according to velocity magnitude. The slab contour interval is 50 km. The red slab contour denotes the base of the rigid corner and the depth of full mechanical coupling between the slab and wedge. Convergence direction is denoted with a black arrow.

gates align approximately parallel maximum stretch directions. On the basis of these observations we use maximum stretch directions as a proxy for seismically fast directions in deformed peridotite. This approximation does not take into account the effects of dynamic recrystallization, which may cause a lag time for the rotation of seismically fast crystallographic directions into the direction of maximum stretch [*Kaminski and Ribe*, 2002; *Kaminski et al.*, 2004]. This lag time becomes especially important in velocity fields that have rapid variations in velocity gradients [*Kaminski and Ribe*, 2002]. The primary focus of this paper is on predicting fabric development in material traveling through the core of the mantle wedge toward the arc mantle. This material encounters relatively consistent deformation gradients in vertical and horizontal planes during the

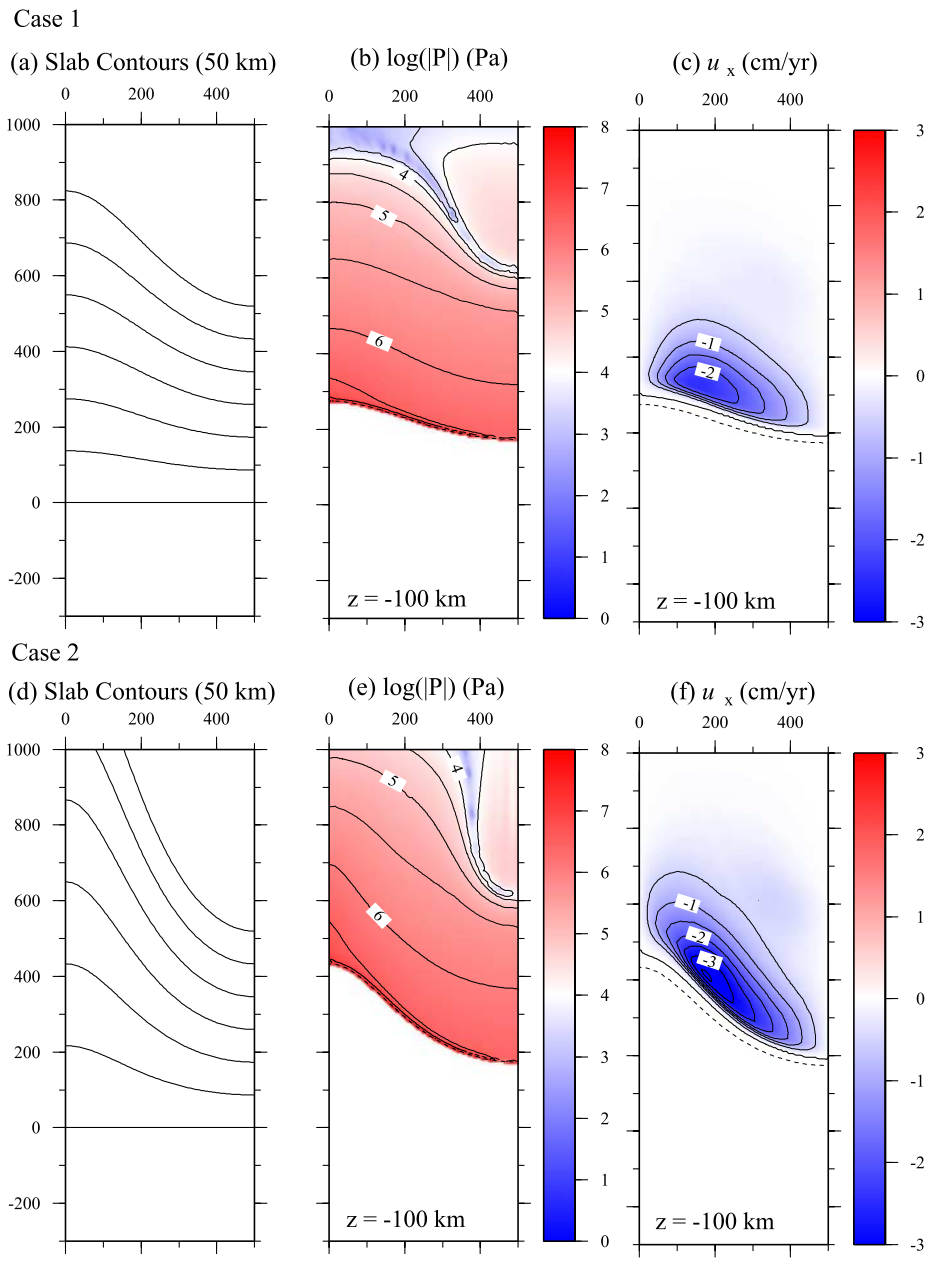

Figure 8. Horizontal cross section showing (a and d) slab geometry, (b and e) the magnitude of dynamic pressure, and (c and f) trench-parallel flow velocity obtained after 20 Ma of subduction for cases 1 and 2 (see Figures 7a and 7b). The magnitude of dynamic pressure rapidly increases toward the corner of the mantle wedge, giving rise to what is referred to in this work as the low-pressure corner. Note that Figures 8b and 8e show the magnitude of the absolute value of dynamic pressure. Dynamic pressure becomes more negative toward the corner of the wedge.

ascent toward the corner of the mantle wedge and trench-parallel stretching is present during almost the entire strain history. Since finite strain is the primary control on fabric development and we are interested in a general qualitative prediction of the pattern of elastic anisotropy, the proxy used in this work is considered sufficient.

[19] Since we are primarily interested in the amount of trench-parallel or convergence-perpendicular stretching, we describe maximum stretch axes with respect to trench geometry. Trench-parallel fabric strength F_{tr} is defined as

$$F_{tr} = \mathbf{v}'_{\max} \cdot \mathbf{v}_{tr} \tag{14}$$

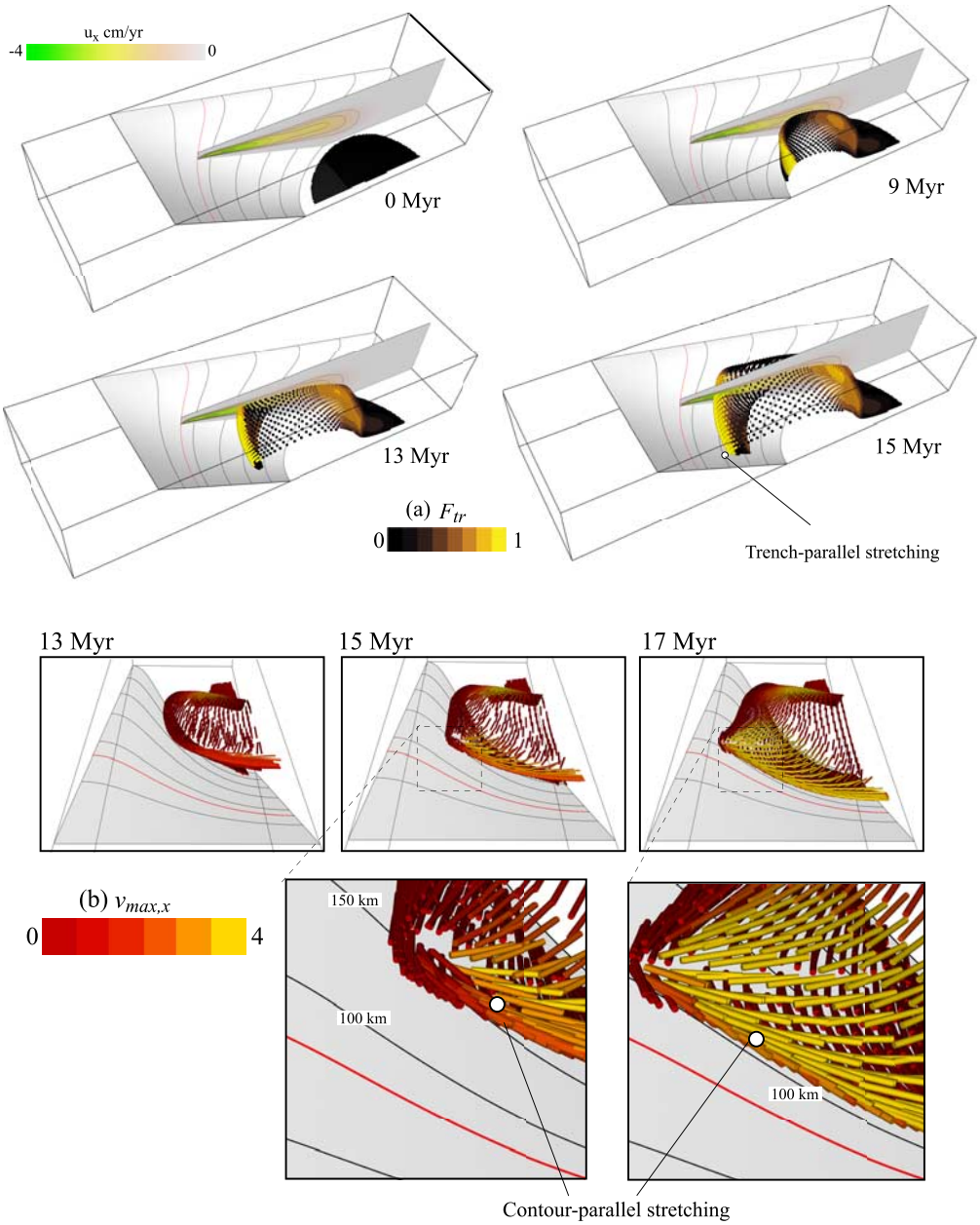

Figure 9. The evolution of finite strain in the steady state flow field for case 2. Finite strain calculations are shown in particles that are initially distributed at the base of the model. This figure shows (a) trench-parallel fabric strength and (b) maximum stretch axes, which are plotted as vectors with a constant length of 50 km and colored according to the magnitude of the x component of maximum stretch axes ($v_{\max,x}$). Note that the trench is parallel to the x axis. $v_{\max,x}$ is a measure of the strength of trench-parallel stretching. Note that time does not refer to the total duration of subduction but instead denotes the duration over which the layer of particles has deformed in the steady state velocity field. Two-dimensional cross sections in Figure 9a show 0.5 cm/a contours of trench-parallel flow velocity (see Figure 6d).

where $\mathbf{v}'_{\max}$ is the unit vector parallel to the maximum stretch axis and $\mathbf{v}_{tr}$ is the unit vector parallel to the trench. When F_{tr} is equal to 1 the maximum stretch axis is parallel to the trench in a horizontal plane. Maximum elongation $e_{\max}$ is used as a proxy for fabric strength and is defined as

$$e_{\max} = \lambda_{\max} - 1 \tag{15}$$

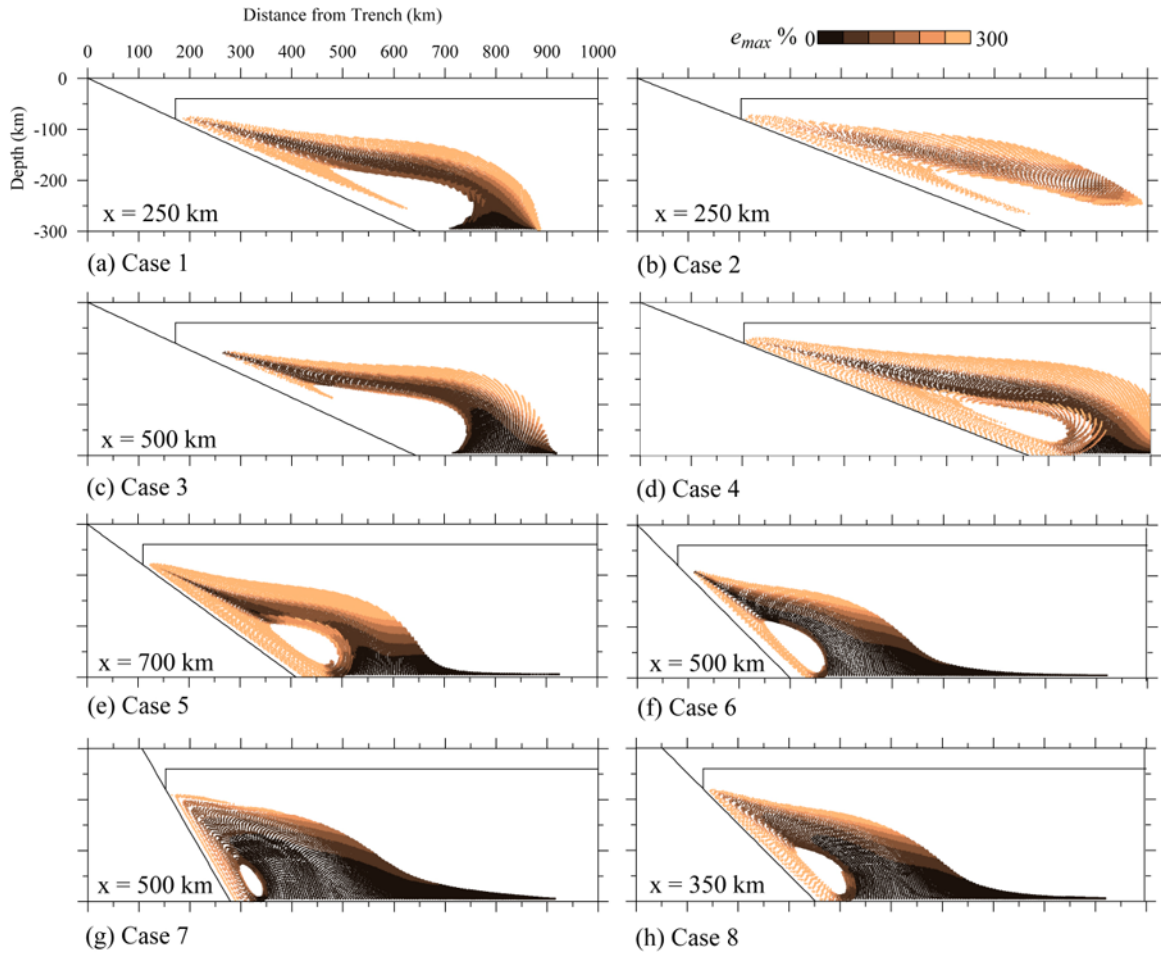

Figure 10. Maximum elongation in particles that are injected into the base of the model every 200,000 years for cases 1–8 (see text). Maximum elongation is used as a proxy for fabric strength.

where λ_{max} is maximum stretch. Experiments [*Zhang et al.*, 2000] and theoretical models of lattice preferred orientation development [*Kaminski et al.*, 2004] show that fabric strength saturates at elongation ranging from 200–500%.

3. Results

[20] In this section we show results from general subduction zone models with a range of geometric parameters observed in subduction systems (Figure 1 and auxiliary material Figures S1–S4). Descriptions of the parameterized slab models for each case are given in Tables 1 and 2 and Figure 3. Models are shown with variable slab dip, curved trenches, oblique subduction and slab edges (Figures 3 and 4). Variable slab dip and curved trenches are described with harmonic functions that produce smooth variations in slab geometry. In many cases harmonic perturbations in slab geometry are truncated along planes of symmetry to reduce computational time. Geometric parameters for specific cases are illustrated in Figures 3a–3d and defined in Table 2.

3.1. Variable Slab Dip

[21] Most subduction systems show 10–20° variations in average slab dip below the seismogenic zone over along-trench distances ranging from 500–1000 km [*Syracuse and Abers*, 2006]. The largest variation in average slab dip over 1000 km is 30° and occurs along the transition from the Japan to Izu-Bonin subduction systems. The largest gradients in slab dip variation occur over distances around 500 km adjacent to flat slab subduction (e.g., N. and S. Andes) [*Anderson et al.*, 2004; *Russo and Silver*, 1994]. Variable slab dip has been proposed as a possible mechanism for strong

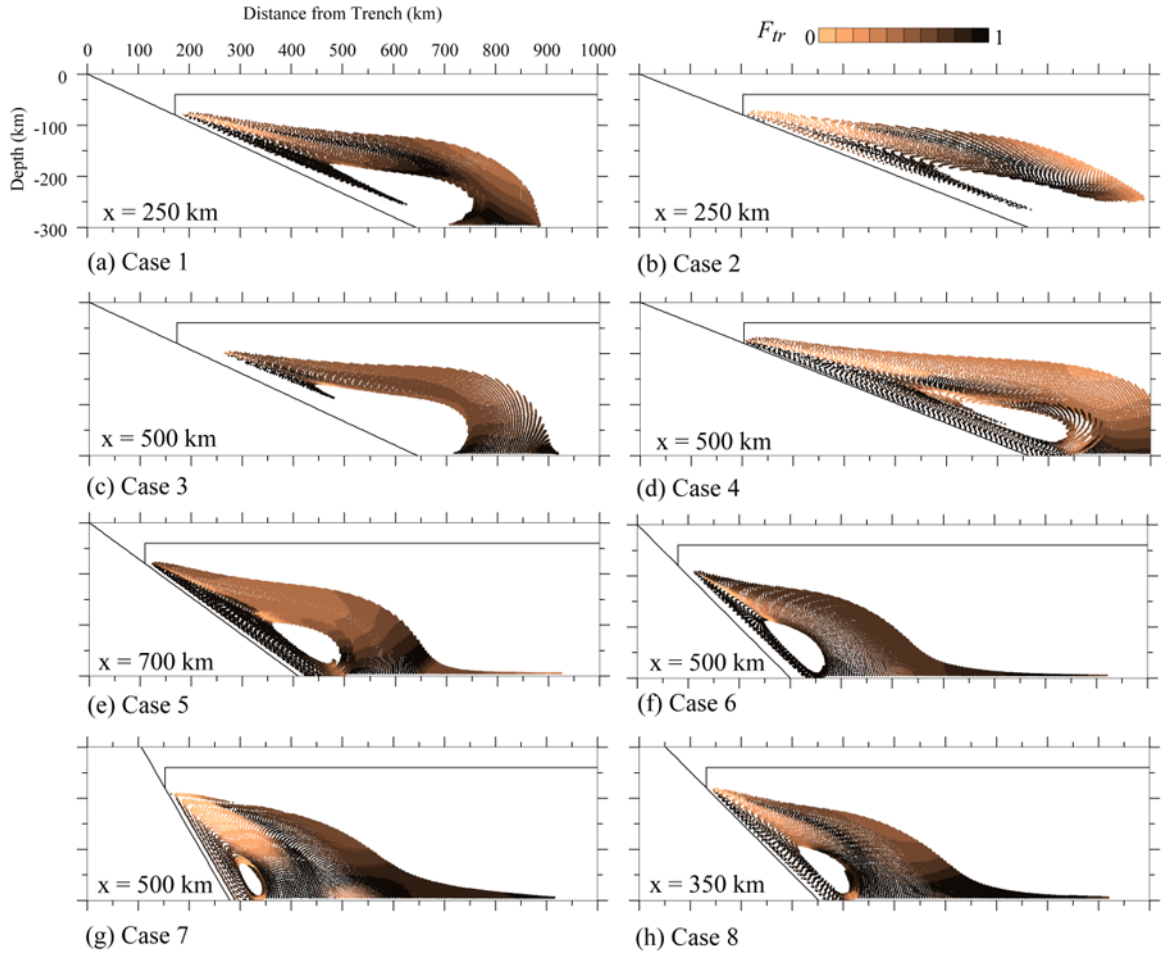

Figure 11. Trench-parallel fabric strength in particles that are injected into the base of the model every 200,000 years for cases 1–8 (see text). Trench-parallel fabric strength is a measure of the trench-parallel alignment of maximum stretch axes (see text).

trench-parallel flow and trench-parallel seismically fast anisotropy [*Hall et al.*, 2000; *Nakajima and Hasegawa*, 2004; *Long and van der Hilst*, 2005]. Figure 7 shows slab geometry and flow lines for cases with along-strike variations in slab dip. These cases address the full range of observed slab dip variations.

3.1.1. Transition to Shallow Slab Dip

[22] Cases 1 and 2 are associated with the largest trench-parallel variations in pressure and magnitude of trench-parallel velocity of all cases presented in this work (Figure 8). Figure 8 shows how the magnitude of dynamic pressure rapidly increases toward the trench giving rise to a low-pressure corner. Shallower dipping slabs push the low-pressure corner further into the back arc and produce larger trench-parallel pressure gradients and larger trench-parallel flow (Figure 8). Trench-parallel velocity is largest within the inflow channel where material travels toward the low-pressure corner of the mantle wedge (Figure 6d). Figures 7a and 7b show that a transition to shallow dipping slabs produces flow lines that differ significantly from two-dimensional cornerflow.

[23] Figures 9a and 9b shows the evolution of trench-parallel stretching in a layer of particles initially distributed at a depth of 300 km for case 2. This layer of particles travels through the steady state velocity field as material flows toward the low-pressure corner. Material in the center of the inflow channel experiences trench-parallel shear, which produces a front of particles with strong trench-parallel stretching (Figure 9a). The magnitude of trench-parallel stretching reaches a maximum of 300–500% beneath the arc mantle (Figure 9b). An animation of strain evolution for case 2 is located in the auxiliary material (Animation 1).

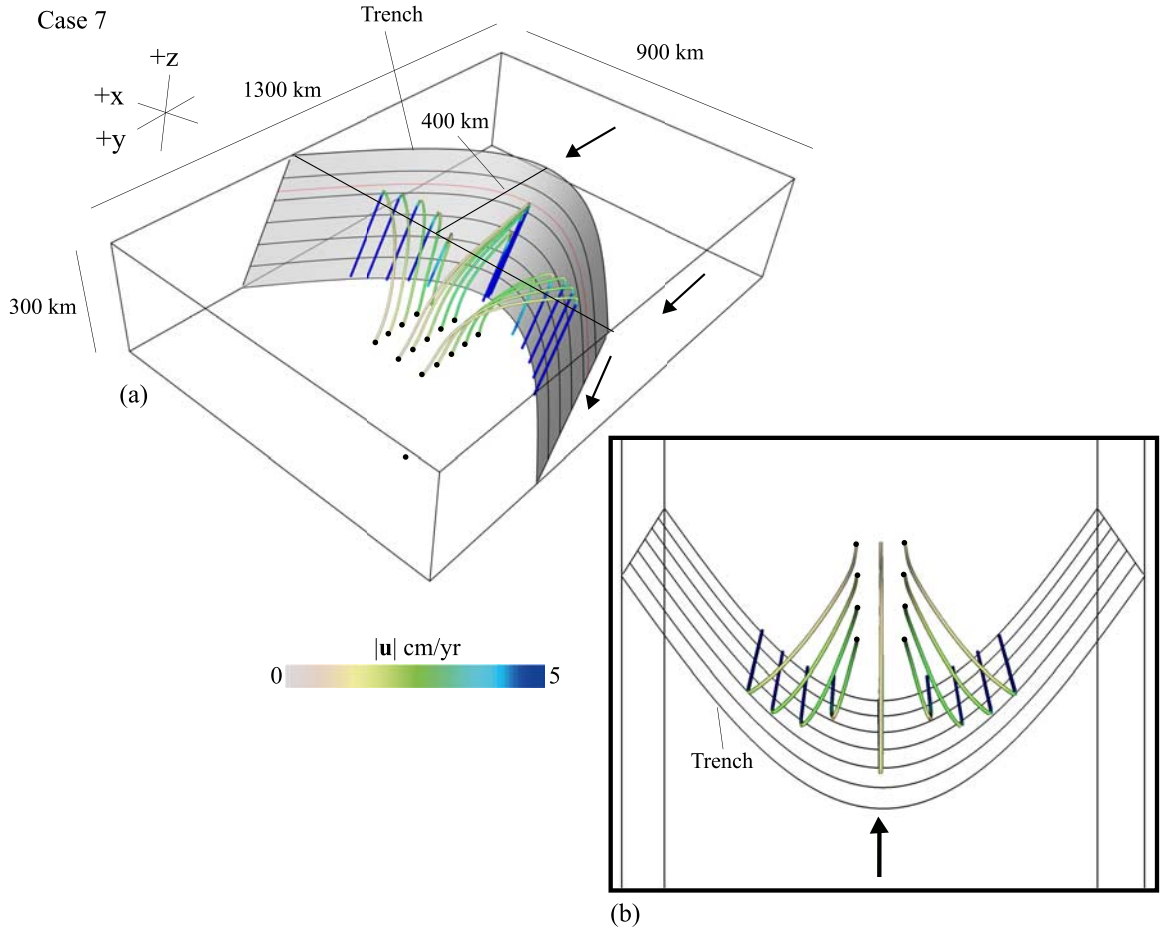

Figure 12. Slab geometry and flow lines for case 7. Flow lines are calculated for particles that were initially distributed parallel to the convergence direction at the base of the model. Flow lines are colored according to velocity magnitude. The slab contour interval is 50 km. The red slab contour denotes the base of the rigid corner and the depth of full mechanical coupling between the slab and wedge. Convergence direction is denoted with a black arrow.

[24] Case 2 is associated with a 30–40 km thick layer of trench-parallel stretching with strain magnitudes ranging from 150–400% (Figures 10b and 11b). This layer develops within the inflow channel of the mantle wedge and could produce trench-parallel splitting with delay times as large as 1 s. Case 1, which has a smaller along-strike dip variation of 10 degrees, is associated with a thinner layer of trench-parallel stretching with smaller magnitudes of strain (Figures 10a and 11a).

[25] The slab geometries of cases 3 and 4 (Figures 7c and 7d) have slab dip variations similar to cases 1 and 2 but over a longer along-strike distance. These models are associated with smaller gradients in slab dip variation and magnitudes of trench-parallel velocity. Case 3 is associated with a minor deviation from cornerflow flow geometry (Figure 7c) and negligible trench-parallel stretching (Figures 10c and 11c). Case 4 involves a broad transition to a shallow dipping slab and is similar to the slab geometry in the northern Andes [*Russo and Silver*, 1994]. This case is associated with a significant deviation from two-dimensional cornerflow (Figure 7d) and a 40–50 km thick layer with strong oblique to trench-parallel stretching (Figures 10d and 11d).

3.1.2. Transition to Moderate Slab Dip

[26] The slab geometries used in cases 1–4 have a transition to shallow dipping slabs with minimum slab dip less than 20°. This slab configuration is associated with a low-pressure region that extends far into the back-arc mantle. A more common situation observed in the world's subduction systems is a transition from relatively steep slabs to shallow dipping slabs with minimum slab dip greater than 30° [*Syracuse and Abers*, 2006]. We address this type of slab configuration with cases 5 and 6 (Figures 7e and 7f).

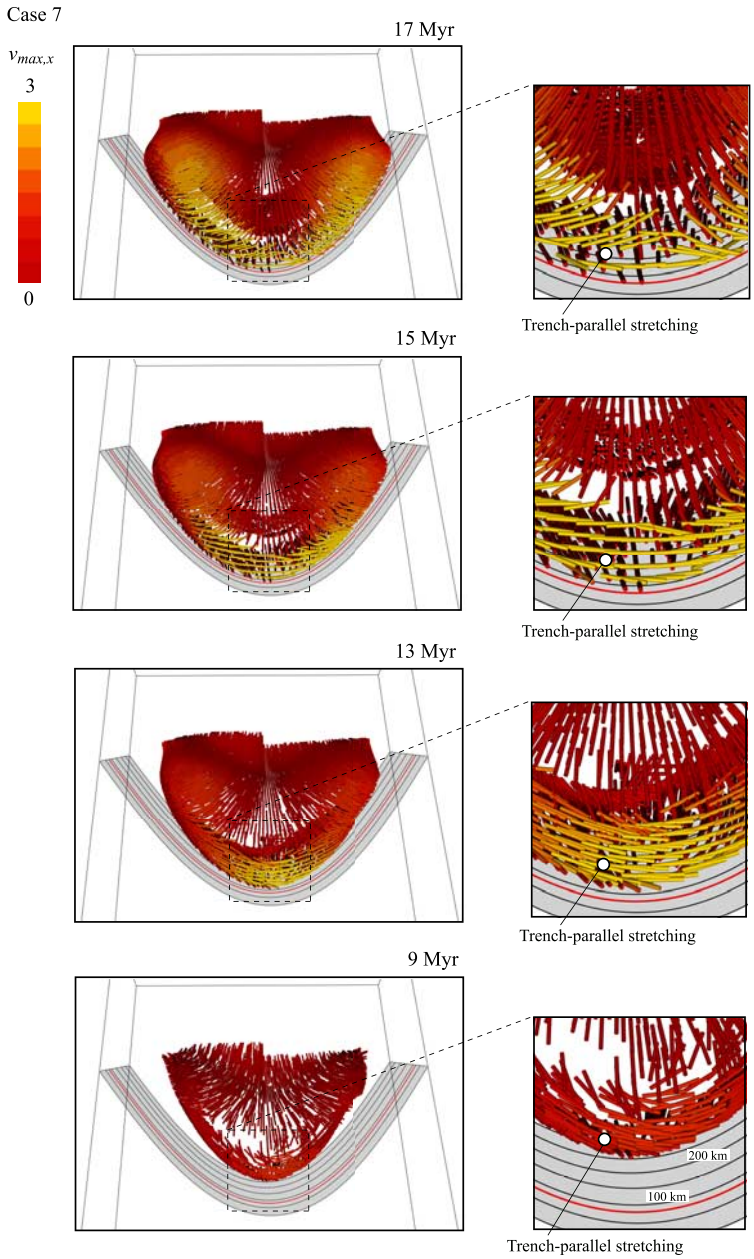

Figure 13. The evolution of finite strain in the steady state flow field for case 7. Finite strain calculations are shown in particles that are initially distributed at the base of the model (see Figure 7). This figure shows maximum stretch axes, which are plotted as vectors with a constant length of 50 km and colored according to the magnitude of the x component of maximum stretch axes ($v_{\max,x}$). $v_{\max,x}$ is a measure of the strength of convergence-perpendicular stretching. Material that flows toward the arc mantle encounters relatively consistent deformation gradients in vertical and horizontal planes, and trench-parallel stretching is present during almost the entire strain history. This suggests that maximum stretch directions are an adequate proxy for seismically fast directions [*Kaminski and Ribe*, 2002]. Note that time does not refer to the total duration of subduction but instead denotes the duration over which the layer of particles has deformed in the steady state velocity field.

[27] Case 5 involves a maximum dip variation of 30° over a length of 1000 km (e.g., Izu-Bonin), whereas case 6 has a maximum slab dip variation of 15° over a distance of 500 km and a constant dip extension of 500 km (e.g., Costa Rica). Both cases 5 and 6 have a relatively small magnitude and uniform distribution of trench-parallel velocity within the center of the inflow channel. This produces a small region with low-magnitude

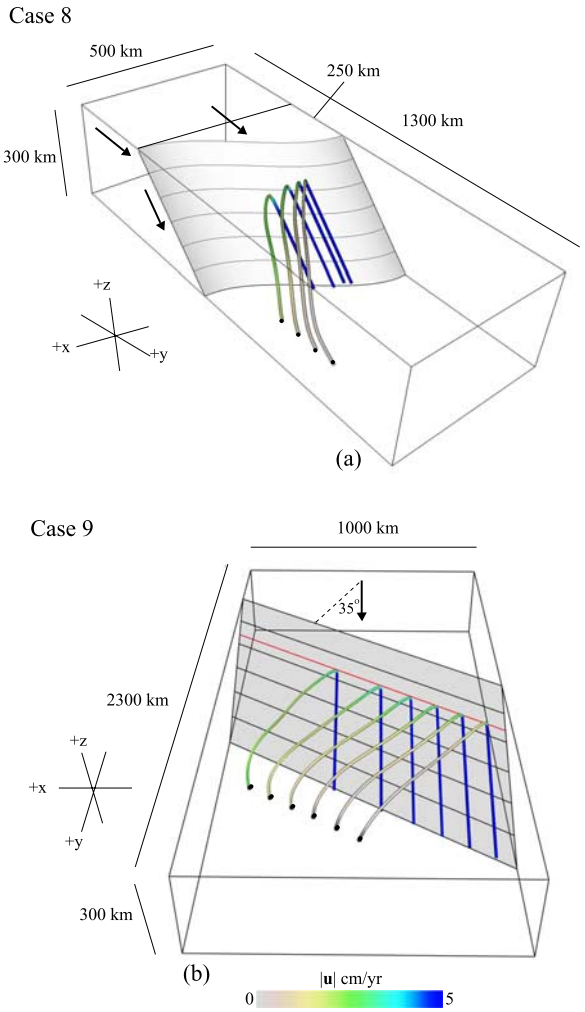

Figure 14. Slab geometry and flow lines for cases (a) 8 and (b) 9. Flow lines in Figure 14a are calculated for particles that were initially distributed parallel to the convergence direction at the base of the model. Flow lines in Figure 14b are calculated for particles initially distributed parallel to the trench. Flow lines are colored according to velocity magnitude.

trench-parallel stretching (Figures 10e, 10f, 11e, and 11f).

3.2. Curved Slabs

[28] Curved slabs and trenches are associated with along-strike variations in the geometry of the low-pressure region in the corner of the mantle wedge. Curved trenches are observed in several subduction systems (e.g., western Aleutians, Alaska, western Ryukyu, Scotia, Lesser Antilles, central Andes, and Marianas). The most extreme examples of trench curvature occur in the Marianas, central Andes, and western Aleutians.

[29] The slab parameters associated with case 7 produce geometric variations similar to those observed in Mariana and western Aleutian subduction systems (Figure 12a). The extent to which flow lines deviate from two-dimensional cornerflow varies along strike giving rise to a radiating flow geometry (Figure 12b). This complex flow geometry produces a 40–60 km thick inclined layer with trench-parallel stretching and maximum elongation greater than 100–200% (Figures 10g and 11g). This trench-parallel stretching develops in a flow field with radiating flow lines that are trench-normal (compare Figure 12b and Figure 13). This model demonstrates that stretching directions inferred from seismically fast orientations may not be indicative of flow direction in three-dimensional systems. An animation of strain accumulation for case 7 is located in the auxiliary material (Animation 2).

[30] The slab geometry used with case 8 has a curved trench that is similar to the central Andean subduction system (Figure 14a). This velocity structure produces moderate trench-parallel shear and stretching in a thin layer with maximum elongation ranging from 150–200% (Figures 10h and 11h).

3.3. Oblique Subduction

[31] Oblique subduction has been proposed by several workers as a cause of strong trench-parallel shear in the mantle wedge [*Hall et al.*, 2000; *Mehl et al.*, 2003]. We test this hypothesis with case 9 (Figure 14b). The slab geometry used with this case includes a straight trench with an oblique orientation with respect to the convergence direction. The normal vector of the trench is oriented 35° relative to the convergence direction. Figure 14b shows flow lines for particles that were initially distributed along a convergence-normal line at the base of the model. Flow lines throughout most of the mantle wedge are approximately perpendicular to the trench. Case 9 shows that return flow within the core of the mantle wedge is primarily controlled by the full coupling point between the slab and wedge, which in turn controls the geometry of the low-pressure corner. Strong oblique stretching is confined to a 25–40 km thick boundary layer above the slab (Figure 15). Maximum stretch directions are oriented perpendicular to the trench throughout most of the inflow channel, a situation similar to two-dimensional cornerflow (Figures 15b and 15c).

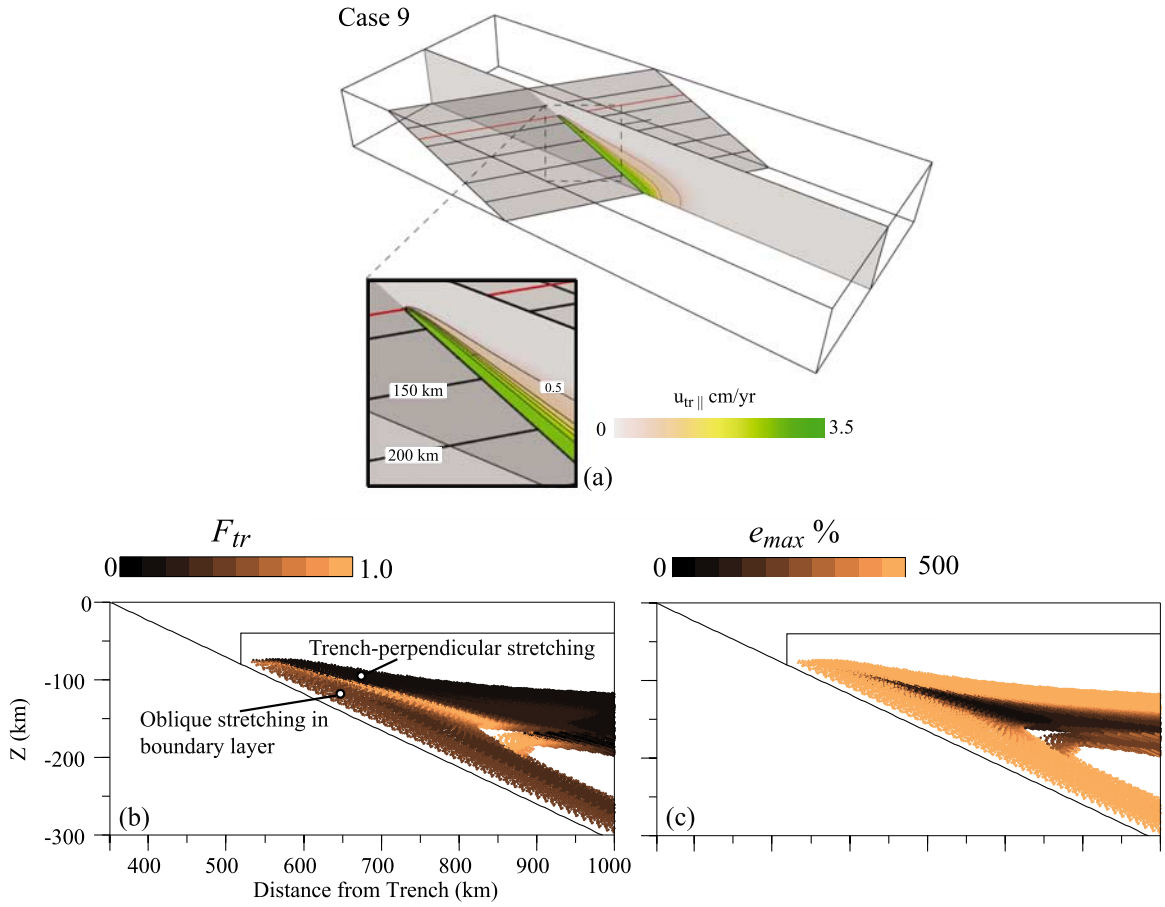

Figure 15. (a) Trench-parallel flow, (b) trench-parallel stretching, and (c) maximum elongation for case 9. Note that oblique shear is not transmitted into the inflow region of the mantle wedge.

3.4. Slab Edges

[32] Figure 16 shows a case with a truncated slab and Newtonian temperature-dependent rheology with 6 orders of magnitude viscosity contrast. With this case strong toroidal flow is generated in the mantle next the low-pressure corner of the mantle wedge. Trench-parallel flow lines extend 50–100 km into the core of the mantle wedge but quickly rotate to trench-normal. Strong focusing and thermal erosion occurs next the truncated slab, which gives rise to locally high temperatures.

4. Discussion and Conclusions

[33] This work addresses a wide range of observed slab geometries including end-member cases. We demonstrate that certain three-dimensional slab geometries can produce significant trench-parallel stretching. These geometries include a transition to shallow dipping slabs with minimum slab dip less than 15–20° (Figures 7b, 9, and 11b) and slabs with strong curvature (Figures 11g, 12, and 13). For both configurations, trench-parallel stretching develops within the inflow channel where material flows toward the low-pressure corner of the mantle wedge. For end-member cases (cases 2 and 7) 20–60 km thick inclined layers with strong trench-parallel stretching develop in the mantle wedge. These regions may be responsible for up to around 1 second of trench-parallel splitting for the range of intrinsic anisotropies observed in naturally deformed peridotite [*Ismaïl and Mainprice*, 1998].

[34] Trench-parallel stretching associated with variable slab dip develops due to a strong component of trench-parallel flow toward the shallow dipping slab. Interestingly, trench-parallel stretching develops in a flow field where flow lines have an oblique not trench-parallel alignment (e.g., Figure 7b). This suggests that seismically fast directions may not be indicative of flow lines in complex three-dimensional systems. Cases with a transition

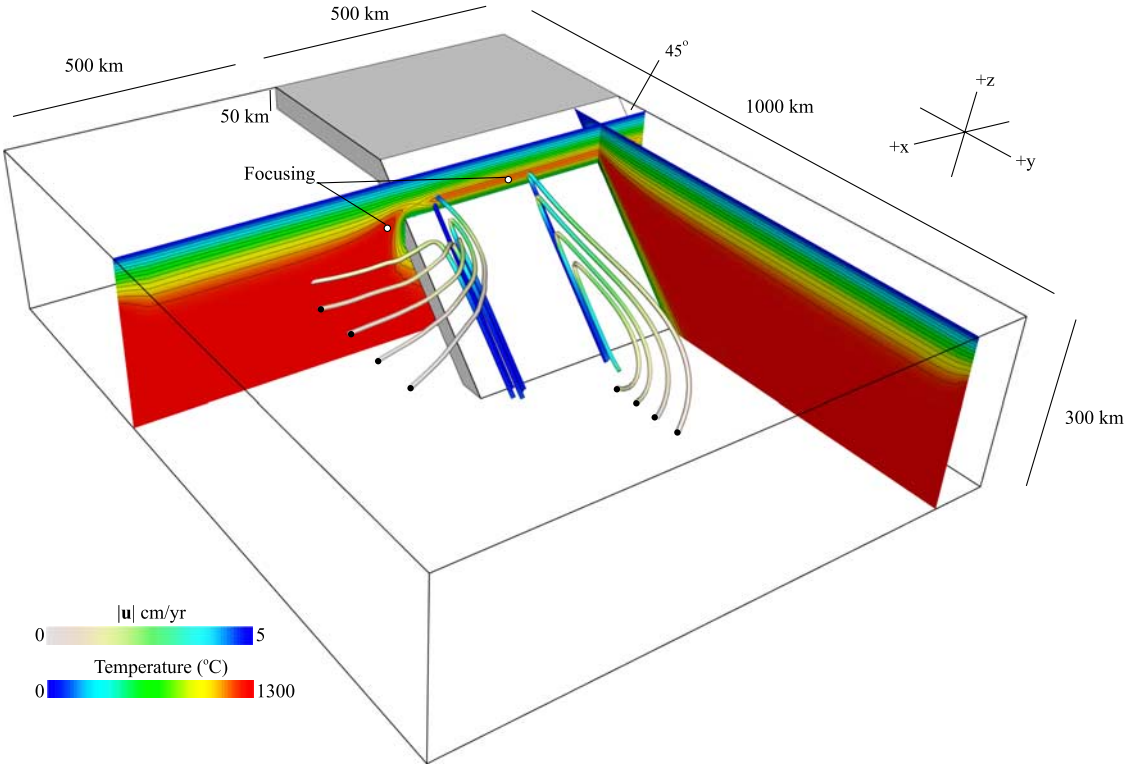

Figure 16. Flow geometry and thermal calculations for case 10.

to shallow dipping slabs with minimum dip less than 15° (cases 2 and 4) have similar geometry to slabs located next to flat slab subduction. Flat slab subduction occurs in several parts of the Andean subduction system [*Russo and Silver*, 1994; *Anderson et al.*, 2004]. The models presented in this work suggest that trench-parallel seismically fast directions observed in these regions [*Anderson et al.*, 2004; M. Anderson et al., Along-strike mantle flow variations in a segment of the South American Subduction zone, Chile and Argentina, submitted to *Earth and Planetary Science Letters*, 2007] may be associated with stretching induced by along-strike variations in slab dip.

[35] The width and amplitude of trench curvature in the Mariana and western Aleutian subduction systems are similar to case 7. This cases is associated with the thickest zone of trench-parallel stretching of all models presented in this work. This trench-parallel stretching develops within a flow field with radiating flow lines that are approximately trench-normal. This case also suggest that stretching directions may be normal to flow lines in subduction zones with large along-strike variations in slab geometry. A more detailed investigation of three-dimensional flow and implications for shear wave splitting in the Andean and Mariana subduction systems will be presented by *Kneller and van Keken* [2007].

[36] One of the largest variations in slab dip occurs in the Izu-Bonin subduction system. Here slab dip varies from 30° to 60° over 1000 km, a slab configuration that is similar to case 5. Both cases 5 and 6 involve large amplitude variations in slab dip with minimum slab dip greater than 30°. These cases are associated with negligible trench-parallel stretching and show that a large variation in slab dip is not sufficient to generate trench-parallel stretching when minimum slab dip is greater than 25–30°.

[37] The southern Kuril and western Java subduction systems are characterized by oblique subduction with a straight trench, a situation that is similar to case 9. Shear wave splitting observations from the hot arc and back arc mantle of the southern Kuril subduction system show trench-normal fast directions. This is consistent with the results of case 9, which suggests that deformation throughout most of the mantle wedge is primarily controlled by the low-pressure corner of the mantle wedge and oblique shear is confined to the boundary layer above the subducting slab (Figure 15). A similar

conclusion was obtained by *Honda and Yoshida* [2005] on the basis of calculated flow geometry.

[38] The strong toroidal flow associated with slab edges (Figure 16) may explain trench-parallel fast directions observed close to slab edges in Taiwan, Kamchatka, northern Tonga, and in southern Japan near the edge of the subducting Philippine Sea Plate. The slab edge model presented in this work predicts that trench-parallel flow will extend only 50–100 km into the mantle wedge. We note that in all of our models we have a steady state geometry. Active flow that includes trench migration and slab roll-back will likely enhance the 3D flow effects and we expect that in this case the converge-normal flow will extend further. The combination of the edge effect and strong slab rollback is a possible source for the strong trench-parallel splitting observed in the Lau basin [*Smith et al.*, 2001].

[39] This work demonstrates that trench-parallel stretching inferred from seismically fast directions may not indicate that flow lines are oriented parallel to the trench. Thick layers with trench-parallel stretching can develop in the mantle wedge when only a component of trench-parallel velocity is present and flow lines have an oblique to trench-normal orientation. This has important implications for the link between flow geometry and shear-wave splitting measurements in systems with large along-strike variations in slab geometry. For end-member cases with transitions to shallow dipping slabs or strong slab curvature, the magnitude of trench-parallel stretching reaches values greater than 100–400% within a seismologically significant volume of the arc mantle.

Acknowledgments

[40] We thank Megan Anderson for discussions on three-dimensional slab geometry and along-strike deformation processes. We also thank Sara Pozgay, Doug Wiens, and James Conder for discussions of trench-parallel anisotropy and flow in the Mariana subduction system. Finally, we thank reviewers Jeroen van Hunen and Thorsten Becker for constructive comments. This research was supported by the National Science Foundation.

References

Anderson, M. L., G. Zandt, E. Triep, M. Fouch, and S. Beck (2004), Anisotropy and mantle flow in the Chile-Argentina subduction zone from shear wave splitting analysis, *Geophys. Res. Lett.*, *31*, L23608, doi:10.1029/2004GL020906.

Behn, M. D., G. Hirth, and P. B. Kelemen (2007), Trench-parallel anisotropy produced by foundering of arc lower crust, *Science*, *317*, 108–111.

Buttles, J., and P. Olson (1998), A laboratory model of subduction zone anisotropy, *Earth Planet. Sci. Lett.*, *164*, 245–262.

Cuvelier, C., A. Segal, and A. A. van Steenhoven (1986), *Finite Element Methods and Navier-Stokes Equations*, 483 pp., D. Reidel, Dordrecht, Netherlands.

Ewart, A., K. D. Collerson, M. Regelous, J. I. Wendt, and Y. Niu (1998), Geochemical evolution within the Tonga-Kermadec-Lau arc-back-arc systems: The role of varying mantle wedge composition in space and time, *J. Petrol.*, *39*, 331–368.

Fischer, K. M., E. M. Parmentier, A. R. Stine, and E. Wolf (2000), Modeling anisotropy and plate-driven flow in the Tonga subduction zone back arc, *J. Geophys. Res.*, *105*, 181–191.

Hacker, B. R., S. M. Peacock, G. A. Abers, and S. D. Holloway (2003), Subduction factory: 2. Are intermediate-depth earthquakes in subducting slabs linked to metamorphic dehydration reactions?, *J. Geophys. Res.*, *108*(B1), 2030, doi:10.1029/2001JB001129.

Hall, C. E., K. M. Fischer, E. M. Parmentier, and D. K. Blackman (2000), The influence of plate motions on three-dimensional back arc mantle flow and shear wave splitting, *J. Geophys. Res.*, *105*, 28,009–28,033.

Hiramatsu, Y., M. Ando, T. Tsukuda, and T. Ooida (1998), Three-dimensional image of the anisotropic bodies beneath central Honshu, Japan, *Geophys. J. Int.*, *135*, 801–816.

Holtzman, B. K., D. L. Kohlstedt, M. E. Zimmerman, F. Heidelback, T. Hiraga, and J. Hustoft (2003), Melt segregation and strain partitioning: Implications for seismic anisotropy and mantle flow, *Science*, *301*, 1227–1230.

Honda, S., and M. Saito (2003), Small-scale convection under the back-arc occurring in the low viscosity wedge, *Earth Planet. Sci. Lett.*, *216*, 703–715.

Honda, S., and T. Yoshida (2005), Effects of oblique subduction on the 3-D pattern of small-scale convection within the mantle wedge, *Geophys. Res. Lett.*, *32*, L13307, doi:10.1029/2005GL023106.

Honda, S., M. Saito, and T. Nakakuki (2002), Possible existence of small-scale convection under the back arc, *Geophys. Res. Lett.*, *29*(21), 2043, doi:10.1029/2002GL015853.

Ismaïl, B. W., and D. Mainprice (1998), An olivine fabric database: An overview of upper mantle fabrics and seismic anisotropy, *Tectonophysics*, *196*, 145–157.

Kaminski, E., and N. M. Ribe (2002), Timescales for the evolution of seismic anisotropy in mantle flow, *Geochem. Geophys. Geosyst.*, *3*(8), 1051, doi:10.1029/2001GC000222.

Kaminski, E., N. M. Ribe, and J. T. Browaeys (2004), D-Rex, a program for calculation of seismic anisotropy due to crystal lattice preferred orientation in the convective upper mantle, *Geophys. J. Int.*, *158*, 744–752.

Karato, S., and H. Jung (2003), Effects of pressure on high-temperature dislocation creep in olivine, *Philos. Mag.*, *83*, 401–414.

Katayama, I., and S. Karato (2006), Effect of temperature on the B- to C-type olivine fabric transition and implications for flow pattern in subduction zones, *Phys. Earth Planet. Inter.*, *157*, 33–45.

Kincaid, C., and R. Griffiths (2003), Laboratory models of the thermal evolution of the mantle during rollback subduction, *Nature*, *425*, 58–62.

Kneller, E. A., and P. E. van Keken (2007), Trench-parallel flow and seismic anisotropy in the Mariana and Andean subduction systems, *Nature*, in press.

Kneller, E. A., P. E. van Keken, S. Karato, and J. Park (2005), B-type olivine fabric in the mantle wedge: Insights from

high-resolution non-Newtonian subduction zone models, *Earth Planet. Sci. Lett.*, *237*, 781–797.

Kneller, E. A., P. E. van Keken, I. Katayama, and S. Karato (2007), Stress, strain, and B-type olivine fabric in the fore-arc mantle: Sensitivity tests using high-resolution steady-state subduction zone models, *J. Geophys. Res.*, *112*, B04406, doi:10.1029/2006JB004544.

Lassak, T. M., M. J. Fouch, C. E. Hall, and E. Kaminski (2006), Seismic characterization of mantle flow in subduction systems: Can we resolve a hydrated mantle wedge?, *Earth Planet. Sci. Lett.*, *243*, 632–649.

Long, M., and R. van der Hilst (2005), Upper mantle anisotropy beneath Japan from shear wave splitting, *Phys. Earth Planet. Inter.*, *151*, 1346–1358.

Long, M., and R. van der Hilst (2006), Shear wave splitting from local events beneath the Ryukyu arc: Trench-parallel anisotropy in the mantle wedge, *Phys. Earth Planet. Inter.*, *155*, 300–312.

Lowman, J. P., L. T. Pinero-Feliciangeli, J.-M. Kendall, and M. H. Shahnas (2007), Influence of convergent plate boundaries on upper mantle flow and implications for seismic anisotropy, *Geochem. Geophys. Geosyst.*, *8*, Q08007, doi:10.1029/2007GC001627.

McKenzie, D. (1979), Finite deformation during fluid flow, *Geophys. J. R. Astron. Soc.*, *58*, 689–715.

Mehl, L., B. R. Hacker, G. Hirth, and P. B. Kelemen (2003), Arc-parallel flow within the mantle wedge: Evidence from the accreted Talkeetna arc, south central Alaska, *J. Geophys. Res.*, *108*(B8), 2375, doi:10.1029/2002JB002233.

Mei, S., and D. L. Kohlstedt (2000), Influence of water on plastic deformation of olivine aggregates: 2. Dislocation creep regime, *J. Geophys. Res.*, *105*, 21,471–21,481.

Nakajima, J., and A. Hasegawa (2004), Shear-wave polarization anisotropy and subduction-induced flow in the mantle wedge of northeastern Japan, *Earth Planet. Sci. Lett.*, *225*, 365–377.

Nakajima, J., J. Shimizu, S. Hori, and A. Hasegawa (2006), Shear-wave splitting beneath the southwestern Kurile arc and northeastern Japan arc: A new insight into mantle return flow, *Geophys. Res. Lett.*, *33*, L05305, doi:10.1029/2005GL025053.

Park, J., and V. Levin (2002), Seismic anisotropy: Tracing plate dynamics in the mantle, *Science*, *296*, 485–489.

Piromallo, C., T. W. Becker, F. Funiciello, and C. Faccenna (2006), Three-dimensional instantaneous mantle flow induced by subduction, *Geophys. Res. Lett.*, *33*, L08304, doi:10.1029/2005GL025390.

Polet, J., P. G. Silver, S. Beck, T. Wallace, G. Zandt, S. Ruppert, R. Kind, and A. Rudloff (2000), Shear wave anisotropy beneath the Andes from the BANJO, SEDA, and PISCO experiments, *J. Geophys. Res.*, *105*, 6287–6304.

Russo, R. M., and P. G. Silver (1994), Trench-parallel flow beneath the Nazca plate from seismic anisotropy, *Science*, *263*, 1105–1111.

Skemer, P., I. Katayama, and S. Karato (2006), Deformation fabrics of the Cima di Gagnone Peridotite Massif, Central Alpes, Swizerland: Evidence of deformation under water-rich conditions at low temperatures, *Contrib. Mineral. Petrol.*, *152*, 43–51.

Smith, G. P., D. A. Wiens, K. M. Fischer, L. M. Dorman, S. C. Webb, and J. A. Hildebrand (2001), A complex pattern of mantle flow in the Lau Back arc, *Science*, *292*, 713–716.

Spencer, A. (1980), *Continuum Mechanics*, 183 pp., Longman, London.

Syracuse, E. M., and G. A. Abers (2006), Global compilation of variations in slab depth beneath arc volcanoes and implications, *Geochem. Geophys. Geosyst.*, *7*, Q05017, doi:10.1029/2005GC001045.

Ulmer, P. (2001), Partial melting in the mantle wedge-the role of H_2O in the genesis of mantle-derived 'arc-related' magmas, *Phys. Earth Planet. Inter.*, *127*, 215–232.

van der Vorst, H. A. (1992), Bi-CGSTAB: A fast and smoothly converging variant of Bi-CG for the solution of nonsymmetric linear systems, *SIAM J. Sci. Comput.*, *12*, 631–644.

van Keken, P. E., B. Kiefer, and S. M. Peacock (2002), High-resolution models of subduction zones: Implications for mineral dehydration reactions and the transport of water into the deep mantle, *Geochem. Geophys. Geosyst.*, *3*(10), 1056, doi:10.1029/2001GC000256.

Wiens, D. A., and G. P. Smith (2003), Seismological constraints on the structure and flow patterns within the mantle wedge, in *Inside the Subduction Factory*, *Geophys. Monogr. Ser.*, vol. 138, edited by J. Eiler, pp. 83–105, AGU, Washington, D. C.

Wolfe, C., and S. C. Solomon (1998), Shear-wave splitting and implications for mantle flow beneath the MELT region of the East Pacific Rise, *Science*, *280*, 1230–1232.

Zhang, S., S. Karato, J. F. Gerald, U. H. Faul, and Y. Zhou (2000), Simple shear deformation of olivine aggregates, *Tectonophysics*, *316*, 133–152.